

THz generation from relativistic plasmas driven by near- to far-infrared laser pulses

J. Déchard,¹ X. Davoine,¹ and L. Bergé^{1,*}

¹CEA, DAM, DIF, F-91297 Arpajon, France

(Dated: September 16, 2019)

Terahertz pulse generation by ultra-intense two-color laser fields ionizing gases with near- to far-infrared carrier wavelength is studied from particle-in-cell (PIC) simulations. For long wavelength (10.6 μm) promoting a large ratio of electron density over critical, photoionization is shown to catastrophically enhance the plasma wakefield, causing a net downshift in the optical spectrum and exciting THz fields with tens of GV/m amplitude in the laser direction. This emission is accompanied by coherent transition radiation (CTR) of comparable amplitude due to wakefield-driven electron acceleration. We analytically evaluate the fraction of CTR energy up to 30% of the total radiated emission including the particle self-field and numerically calibrate the efficiency of the matched blowout regime for electron densities varied over three orders of magnitude.

PACS numbers: 52.25.Os, 42.65.Re, 52.38.Hb

The ability of terahertz (THz) waves to probe matter is attracting interest for lots of applications reviewed, e.g., in [1]. Recently, novel challenges such as compact THz electron accelerators [2–4] or THz-triggered chemistry [5] raised the need of mJ THz pulses with high field strength $> \text{GV/m}$. Optical rectification in organic crystals [6] or using tilted-pulse-front pumping [7] can achieve percent conversion efficiency and sub-mJ THz energies with few 0.1 GV/m field strengths. These solid-based technologies, however, remain limited by damage thresholds. In contrast, gas plasmas created by intense, two-color laser pulses may supply suitable emitters free of any damage [8]. Electrons are tunnel-ionized by the asymmetric light field usually composed of a near-IR fundamental wavelength (800 nm) and its second harmonic (400 nm). Their “photocurrent” polarized in the laser direction generates a broadband photocurrent-induced radiation (PIR) in the THz range [9]. Nevertheless, two-color setups using moderate intensities $\sim 10^{14} \text{ W/cm}^2$ only achieve conversion efficiencies $< 10^{-3}$ and μJ energies [10, 11].

In the relativistic regime, however, when the normalized vector potential $a_0 \equiv 8.5 \times 10^{-10} I_0^{1/2} [\text{W/cm}^2] \lambda_0 [\mu\text{m}]$ is larger than unity (I_0 is the intensity and λ_0 denotes the laser wavelength), plasma waves trigger a strong longitudinal field exploited for laser-wakefield acceleration (LWFA) [12]. Accelerated electrons crossing the plasma-vacuum interface can then emit coherent transition radiation (CTR) operating in the THz band. Leemans et al. [13, 14] reported THz energy of 3-5 nJ per pulse measured from a dense gas jet of helium. Theoretical estimates assuming a Boltzmann distribution of 4.6 MeV confirmed this energy yield and anticipated the possibility to provide few 100 μJ energies by increasing the electron bunch to tens of MeV and/or the plasma diameter to mm scales. Record values were later achieved in numerical simulations from which CTR took over PIR by delivering conversion efficiencies $> 5 \times 10^{-3}$ and mJ THz pulse energies [15]. Such performances have been reached in laser-solid experiments [16, 17].

Besides, mid- and far-infrared light sources supplying TW peak powers are today available. Femtosecond laser facilities with 3.9 μm central wavelength opened the way to multi-octave supercontinuum generation [18] and can accelerate electrons to 12 MeV energy in gas jets [19]. CO₂ lasers ($\lambda_0 = 10.6 \mu\text{m}$) are also operational in the ps range [20] and they should soon provide revolutionary tools unveiling new regimes in particle acceleration and future colliders [21]. Therefore, it is worth investigating the gain that such optical sources may offer in THz science, since their carrier wavelength is already close to the spectroscopy range of interest. Several studies [22–25] highlighted the impressive growth in the THz energy yield when increasing the pump wavelength of two-color-gas setups at moderate intensities. Relativistic interactions remain to be explored for this purpose.

The content of this Letter is threefold. First, along the laser polarization axis, we report from PIC simulations a drastic change in the laser-to-THz conversion process when long-wavelength pulses interact with gases in relativistic regime. The underlying mechanism differs from both PIR and CTR: Here, ionization fronts increase the ponderomotive pressure and catastrophically enhance the plasma waves, which, in the self-modulated (SM) LWFA regime, downshift the laser spectrum to low frequencies $< 10 \text{ THz}$. Second, in the radial direction, better electron injection gives rise to a strong CTR field with comparable amplitude $\sim 20 \text{ GV/m}$. Third, we quantify the radiated energy for electron densities over critical covering three decades and provide an estimate of the CTR yield disconnected from the particle self-field.

Simulations are performed with the PIC, kinetic code CALDER [26, 27] solving Maxwell-Vlasov equations with strong-field ionization [28] in 2D planar geometry. The longitudinal (transverse) axis is set along x (resp. y), while the laser pulse is linearly polarized in the z direction. We here consider three fundamental wavelengths: $\lambda_0 \equiv 2\pi c/\omega_0 = 0.8, 3.9$ and $10.6 \mu\text{m}$ for the same laser potential $a_0 = 2.2$, associated to the input intensities

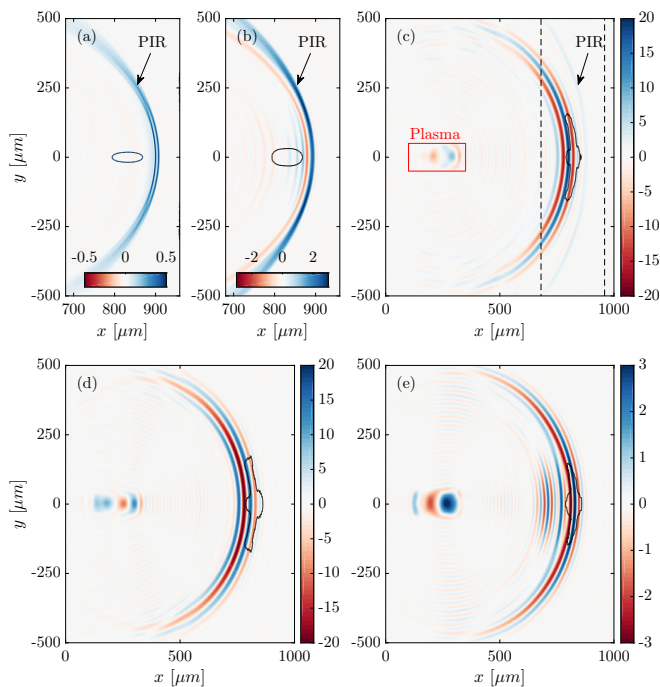


FIG. 1. (a-c) Electric field E_z (color bars in GV/m) produced by a two-color Gaussian pulse with $a_0 = 2.2$ ionizing He, filtered in the range $\nu < \nu_0/3$ and transmitted to vacuum at $t = 3200$ fs ($500 \mu\text{m}$ after the plasma channel, see [29]) for $\lambda_0 =$ (a) 0.8 , (b) 3.9 and (c) $10.6 \mu\text{m}$. Arrow points to the PIR field. In (c) the black dashed rectangle indicates the simulation domain of (a,b) encompassing the laser region; the red rectangle delineates the plasma volume. (d,e) show the same field pattern for (d) a single-color pulse and (e) a pre-ionized plasma at $10.6 \mu\text{m}$. Gray contours are eye-guides for the laser pulse envelope undergoing distortions along propagation.

$I_0 \simeq 10.5$, 0.44 and $0.06 \times 10^{18} \text{ W/cm}^2$, respectively. The input pulse is Gaussian in time and space with its two harmonics ($\omega_0, 2\omega_0$) having the same FWHM duration $\tau_0 = 150$ fs and FWHM transverse width w_0 varying between 20 and $50 \mu\text{m}$. The intensity ratio between the two harmonics is 10% and their initial phase shift is $\pi/2$. The two-color field is focused into a gas cell of helium with atomic density $n_a = 5.5 \times 10^{17} \text{ cm}^{-3}$, along a trapezoidal density profile of length L_p with $200 \mu\text{m}$ -long plateau and $25 \mu\text{m}$ ramps. The plasma wavelength is $\lambda_p = \sqrt{n_c/n_e} \lambda_0$, where $n_c \simeq 1.11 \times 10^{21}/\lambda_0^2 [\mu\text{m}]$ is the critical density and n_e denotes the electron density. The ratio n_e/n_c in He thus increases from 6.3×10^{-4} to 0.11 for $0.8 \leq \lambda_0 \leq 10.6 \mu\text{m}$ while $\lambda_p = 32 \mu\text{m}$. The frequency window chosen to extract the THz waveforms is $\nu \equiv \omega/2\pi < \nu_0/3$, which is performed by inverse Fourier Transform using a 6th-order hyperGaussian filter.

Laser-polarized THz field - Figure 1(a) shows a snapshot of the z -polarized THz field for $\lambda_0 = 0.8 \mu\text{m}$ at $500 \mu\text{m}$ after the plasma-vacuum interface. Two PIR peaks emerge with about 0.5 GV/m maximum amplitude. When increasing the laser wavelength to $\lambda_0 = 3.9$

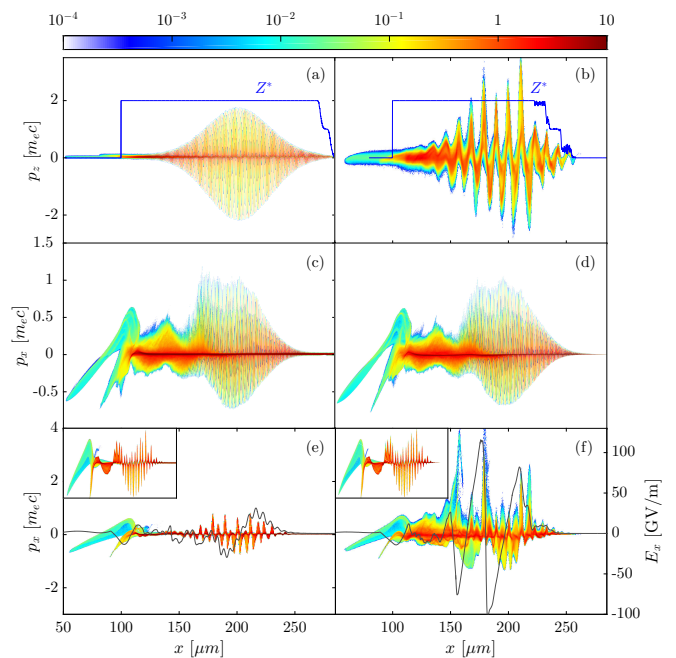


FIG. 2. (a,b) Transverse momentum at $t = 1100$ fs for $\lambda_0 =$ (a) 0.8 and (b) $10.6 \mu\text{m}$. The blue curves show the ionization degree of He. (c,d) Longitudinal momentum for $\lambda_0 = 0.8 \mu\text{m}$ in (c) pre-ionized helium and (d) helium undergoing ionization. (e,f) same information for $\lambda_0 = 10.6 \mu\text{m}$. Gray curves display the longitudinal electric field (right axis). Insets show the same phase space (x, p_x) for hydrogen ($n_e = n_a$).

μm , the PIR becomes more efficient since the electron transverse momentum, p_z , and related current density linearly scale with λ_0 [30], which is confirmed by the field strength (3 GV/m) of Fig. 1(b). With $\lambda_0 = 10.6 \mu\text{m}$, however, photocurrents only deliver the first wavefront on the right-hand side of Fig. 1(c), being much weaker than expected ($\sim 2 \text{ GV/m}$, see arrow). This sudden drop of PIR is attributed to the fall in the photocurrent efficiency, decreased as the ionization sequences develop together with the wakefield. Surprisingly, a multi-cycle THz pulse localized behind the PIR with 20 GV/m field strength and $\sim 7 \text{ THz}$ oscillation frequency emerges, which seems triggered by another process as its location, emission angle and amplitude are different. To tackle this THz waveform, other simulations have been performed with one color only, yielding a similar pattern without the PIR field [Fig. 1(d)]. Furthermore, when simulating a pre-ionized plasma, the THz field strength decreases by a factor ~ 6 [compare color bars of Figs. 1(c) and 1(e)]. Hence, for long-wavelength pumps, photoionization keeps a non-trivial impact on the transverse THz emission, but its action differs from the standard PIR mechanism.

Proving the importance of photoionization, Figs. 2(a,b) display the (x, p_z) electron phase space when the laser is fully inside the plasma for $\lambda_0 = 0.8$ and $10.6 \mu\text{m}$, respectively. The blue curves plot the growth in the ion

charge Z^* along the optical path. At each ionization instant, freed electrons acquire a kick in their transverse momentum p_z , linked to the laser vector potential [31]. For $\lambda_0 = 0.8 \mu\text{m}$, the transverse drift momentum initiated by ionization and exiting the rear pulse is small. In contrast, for the $10.6 \mu\text{m}$ pulse, p_z reaches higher values in the ionization zone. Figures 2(c-f) compare the longitudinal phase space (x, p_x) at the same time in pre-ionized or initially-neutral helium. The longitudinal momentum develops two characteristic oscillations, i.e., the $\sim 2\omega_0$ fast component of the laser ponderomotive force and the plasma frequency $\sim \omega_p$. The plasma wave modulates the pulse envelope in the SM-LFWA regime since $c\tau_0 = 45 \mu\text{m} > \lambda_p$. No noticeable change occurs at $0.8 \mu\text{m}$, whether or not ionization is acting, due to weak momentum transfer. However, compared with pre-ionized He, p_x with $\lambda_0 = 10.6 \mu\text{m}$ reaches much higher values, up to $5 m_e c$ [Fig. 2(f)], and thus increases the electrostatic field that develops a sawtooth-like nonlinear plasma wave. Photoionization hence directly impacts the wakefield dynamics, in particular by increasing the ponderomotive pressure exerted on the plasma by particles born at rest [29, 31]. Insets in Figs. 2(e,f), showing no change for a hydrogen gas, indeed evidence that amplification of the plasma waves in He requires secondary ionization events after the formation of the wakefield. These properties are justified in [29] by means of a 1D, quasi-static model accounting for ionization in the transverse and longitudinal momenta of the plasma wave.

Figure 3(a) illustrates the PIC on-axis longitudinal and transverse field in ionized He. The THz field is centered near the relativistic plasma frequency $\tilde{\nu}_p \equiv \nu_p/\sqrt{\gamma} \sim 7$ THz of the wakefield modulating the rear pulse, where γ denotes the electron Lorentz factor. The feedback of the sharp plasma wave fluctuations on the laser pulse nonlinearly modifies the optical refractive index, $\eta \approx \sqrt{1 - n_e/n_c\gamma}$, which promotes the creation of new wavelengths [32]. The ponderomotive force accumulates electrons, which decreases the pulse group velocity (photon deceleration) and leads to local redshifts. Figure 3(b) shows the Wigner transform of the on-axis laser electric field near the exit of the plasma channel. We clearly observe a frequency downshift ($\partial_x k < 0$) at the top of the plasma out-ramp induced by the propagation in the plasma along which the gradients in the refractive index, $\eta \partial_x \eta = -\frac{1}{2} \partial_x n_e/n_c\gamma \propto \partial_x k$, are also detailed. In the frequency domain, Fig. 3(c) shows the log-log amplitude spectrum of the transverse field transmitted to vacuum for the mid-IR fundamental wavelengths investigated. Unlike the $3.9 \mu\text{m}$ pump, the $10.6 \mu\text{m}$ laser spectrum (black curves) widely broadens between 1 and 100 THz around the pump wave and develops a net enlargement around the plasma frequency. With a ratio n_e/n_c equals to 0.11, Raman instabilities modulate the laser pulse prior to wakefield acceleration in the bubble regime [33]. The latter is attained when the pulse width

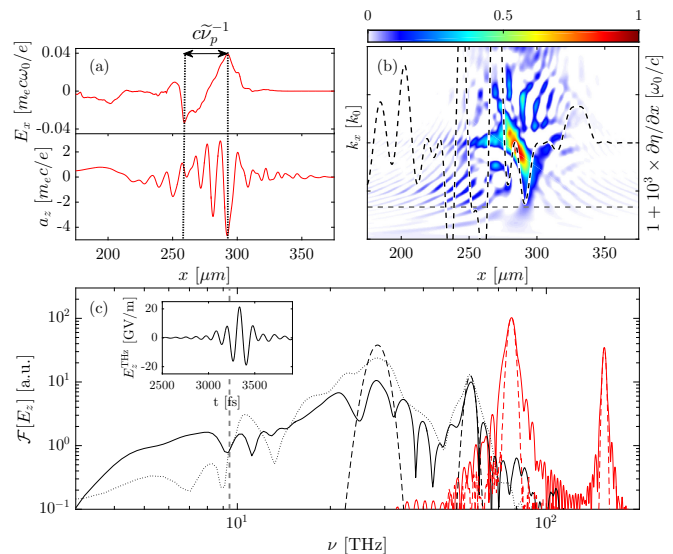


FIG. 3. (a) On-axis PIC longitudinal field (top) and transverse vector potential (bottom) at $t = 1400$ fs. (b) Wigner Transform $\mathcal{W}_E(x, k) = \int_{-\infty}^{+\infty} E(x+x'/2)E^*(x-x'/2)e^{-ikx'} dx'$ of the on-axis two-color laser electric field for $\lambda_0 = 10.6 \mu\text{m}$ along with the gradient of the refractive index computed from the ratio $n_e/n_c\gamma$ using PIC simulation data (dotted black curves). The dashed line indicates the cut-off frequency (9.33 THz) and wavenumber. (c) On-axis log-log scaled spectrum of E_z at the entrance of the simulation domain (dashed black curves) and at $x = 840 \mu\text{m}$ (solid curves) for ionized He. Inset: THz field. Red curves: $3.9 \mu\text{m}$, black curves: $10.6 \mu\text{m}$. The dotted black curve shows the on-axis spectrum for $10.6 \mu\text{m}$ in preionized helium.

is close to $(\lambda_p/\pi)\sqrt{a_z}$ [34] and high-field values $a_z > 4$ are reached by self-focusing [see Fig. 4(a)]. The optical spectrum then slips down to less than 8 THz. Figure 3(c) evidences that the photon redshift around $\tilde{\nu}_p \simeq 7$ THz is particularly marked when ionization is activated. This mechanism explains the THz field patterns of Fig. 1(c) and we evaluate its efficiency to 1.2% in the frequency window $\nu < 9.5$ THz.

Radially-polarized THz field - High amplitudes in the longitudinal field [Fig. 2(f)] promote particle injection. Using longer laser wavelengths also favors self-focusing for peak powers above critical, $P > P_c = 17(\lambda_p/\lambda_0)^2[\text{GW}]$, and increases the charge of the accelerated electron bunch [19]. Figure 4(a) shows the maximum normalized laser electric field along the propagation axis for the three studied wavelengths. The 0.8 and $3.9\text{-}\mu\text{m}$ pumps do not self-focus due to the weak ratio n_e/n_c . In contrast, a clear sequence of collapse and plasma blowout occurs at $\lambda_0 = 10.6 \mu\text{m}$, where the intensity is amplified by a factor ~ 4 and reinforced by pulse steepening through multi-ionization of He. Photoionization thus accelerates the bubble formation. As a result, the laser spot enters the blowout wakefield regime [34] leading to electron injection into a well-shaped bubble

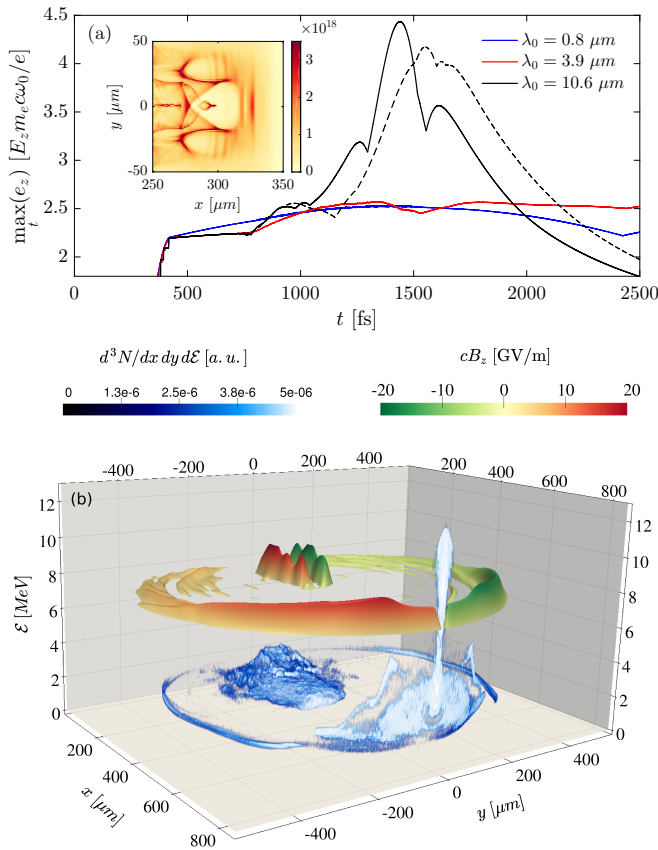


FIG. 4. (a) Maximum normalized two-color laser field amplitude for the three wavelengths λ_0 . The dashed curve shows e_z for pre-ionized helium when $\lambda_0 = 10.6 \mu\text{m}$. Inset displays a plasma bubble where electron injection takes place at the plasma exit ($t = 1400$ fs). (b) Density map (blue colormap) in the phase space (x, y, \mathcal{E}) at $t = 2500$ fs, where \mathcal{E} [MeV] denotes the electron energy. On top of it the radiated CTR magnetic field cB_z [GV/m] is plotted (green-red colormap).

[see inset of Fig. 4(a)]. Later, this electron bunch will pass the plasma-vacuum boundary, generating a CTR field radiating in the THz range [13, 15]. To visualize the correlation between the accelerated particles and the CTR field, Fig. 4(b) shows a map revealing three distinct populations of electrons. The first one constituting the plasma channel has rather low energy and is located near axis at $y \approx 0$, $x \leq 400 \mu\text{m}$ (see blue area). The second electron population forms the expanded bubble outside the plasma at $y \approx \pm 400 \mu\text{m}$. At $x \simeq 700 \mu\text{m}$, the third, wakefield-accelerated electron population reaches an energy as high as 12 MeV. The CTR field generated by the escaping electrons is represented in 2D by the z -polarized magnetic field $B_z = \int (\partial_y E_x - \partial_x E_y) dt$ (green-red colormap). This single-cycle field has a maximum amplitude of about 20 GV/m and corresponds to 1.4% conversion efficiency ($\nu < 9.5$ THz). Associated to 3D laser pulses with 222 mJ input energy (focal spot radius equal to w_0), this THz field may thus contain ~ 3 mJ en-

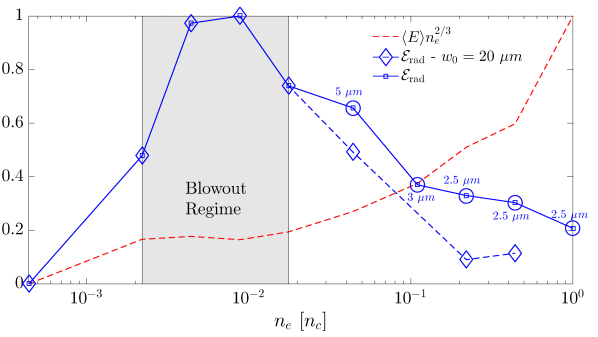


FIG. 5. THz energy in the range $\nu < 0.3 \nu_0$ (blue solid lines) normalized to its maximum value (39 mJ) for 1- μm single-color pump at $x = 500 \mu\text{m}$ from the vacuum-plasma interface and $\langle E \rangle n_e^{2/3}$ (red dashed line) extracted from PIC simulations as function of the electron density (n_e). Blue circles specify values of the laser waist decreased from 20 μm to avoid filamentation. Gray area delineates the blow-out regime.

ergy. Such CTR pulses, radially-polarized in 3D, could be distinguished from the former laser-polarized THz component by using a THz analyzer handling ellipticity [35].

Finally, we parametrically scan the impact of the density ratio n_e/n_c , previously varied through λ_0 , on the transition radiation. Because CTR is mainly driven by the fundamental pump, we simulate a single-color 1- μm , 35-fs FWHM laser pulse with 3.7 J energy using the CALDER-CIRC code [15]. The density ratio is increased from $n_e/n_c \simeq 4.5 \times 10^{-4}$ up to unity. Accordingly, λ_p decreases from 47 μm down to 1 μm , while the laser pulse resonantly excites the wakefield whenever $\lambda_p \sim 10 \mu\text{m}$, i.e., $n_e/n_c \sim 10^{-2}$. Our simulations are constrained by a constant areal density, $n_e L_p = 7.8 \times 10^{17} \text{ cm}^{-2}$, for treating the same electron number in the longitudinal direction. To keep a unique electron bunch, the transverse beam waist may be decreased when the highest density ratios lead to multiple filamentation ($P/P_c > 10$).

Figure 5 summarizes the radiated energy computed from ten plasma densities (blue curve). The dashed red curve plots variations in the product of the mean electron energy $\langle E \rangle$ and $n_e^{2/3}$, expected to be constant in the matched blowout regime [34]. Maximum radiated field is reached in this regime and field emission by wakefield-accelerated electrons only varies by a factor ~ 5 over three plasma decades. For $n_e/n_c > 10^{-2}$, electron acceleration enters the SM-LWFA regime implying a drop in the energy yield, which is reinforced by multiple filamentation occurring with large waist ($w_0 = 20 \mu\text{m}$, dashed blue curve). Inspection of data reveals the generation of up to 50 GV/m electric fields (not shown).

These impressive field values are, however, produced by both the CTR component further reaching the detector and the self-field of the accelerated electrons. The splitting time t_s necessary for separating the CTR field propagating at c in vacuum and the self-field of an elec-

tron bunch with μm length L_b is typically $t_s \approx 2\gamma^2 L_b/c$ [36], requiring mm length scales that are barely accessible in PIC simulations. Evaluating the magnetic field from the Biot-Savart equation applied to a uniform bunch with zero radius enables us to separate the CTR energy from the remaining radiated energy. This analysis, performed in [29], extracts the fraction of CTR yield, which is found to remain within 20 – 30% of the total radiated energy. This result invites us to decrease all our previous CTR field amplitudes and energies by a factor ~ 2 and ~ 4 , respectively. These energy estimates remain larger than Leemans et al.’s measurements, as the acceleration schemes exploited in [13] used plasma lengths exceeding far the electron dephasing length $\sim \gamma^2 \lambda_p$ and were out of the optimum blowout regime.

In summary, we demonstrated that photoionization matters when long laser wavelengths are employed to create intense THz fields in relativistic plasmas. First, the ionization-induced pressure is non zero from the second electron extraction, which increases the plasma wakefield and cause photon deceleration. This dynamics generates high THz fields through frequency downshifts in the optical spectrum. Second, CTR by the wakefield accelerated electrons is enhanced by more efficient self-focusing. We endly evaluated the fraction of CTR energy in gases up to $\sim 30\%$ of the overall radiation emitted in the near-field and demonstrated that the blowout regime provides the highest wakefield-accelerated energy yield. A laser-to-THz conversion efficiency close to the percent could be reached, demonstrating another relevance of CO₂ lasers in relativistic laser-plasma interaction.

ACKNOWLEDGEMENT

The authors acknowledge L. Gremillet, G. Sary and A. Debayle for fruitful discussions as well as GENCI France for awarding us access to the supercomputer CURIE using Grant # A0010506129.

* luc.berge@cea.fr

- [1] L. Bergé, K. Kaltenecker, S. Engelbrecht, A. Nguyen, S. Skupin, L. Merlat, B. Fischer, B. Zhou, I. Thiele, and P. U. Jepsen, *EuroPhys. Lett.* **126**, 24001 (2019).
- [2] E. A. Nanni, W. R. Huang, K.-H. Hong, K. Ravi, A. Fallahi, G. Moriena, R. J. D. Miller, and F. X. Kärtner, *Nat. Commun.* **6**, 8486 (2015).
- [3] A. Sharma, Z. Tibai, J. Hebling, and J. A. Fülöp, *J. Phys. B: At. Mol. Opt. Phys.* **51**, 204001 (2018).
- [4] A. Curcio, A. Marocchino, V. Dolci, S. Lupi, and M. Petrarca, *Scient. Reports* **8**, 1052 (2018).
- [5] J. L. LaRue, T. Katayama, A. Lindenbergh, A. S. Fisher, H. Öström, A. Nilsson, and H. Ogasawara, *Phys. Rev. Lett.* **115**, 036103 (2015).
- [6] C. Vicario, B. Monoszalai, and C. Hauri, *Phys. Rev. Lett.* **112**, 213901 (2014).
- [7] J. A. Fülöp, Z. Ollmann, C. Lombosi, C. Skrobel, S. Klingebiel, L. Pálfalvi, F. Krausz, S. Karsch, and J. Hebling, *Opt. Express* **22**, 20155 (2014).
- [8] H. A. Hafez, X. Chai, A. Ibrahim, S. Mondal, D. Férachou, X. Ropagnol, and T. Ozaki, *J. Opt.* **18**, 093004 (2016).
- [9] K.-Y. Kim, A. J. Taylor, J. H. Glowonia, and G. Rodriguez, *Nature Photon.* **2**, 605 (2008).
- [10] T. I. Oh, Y. S. You, N. Jhajj, E. W. Rosenthal, H. M. Milchberg, and K.-Y. Kim, *Appl. Phys. Lett.* **102**, 201113 (2013).
- [11] C. Meng, W. Chen, X. Wang, Z. Lü, Y. Huang, J. Liu, D. Zhang, Z. Zhao, and J. Yuan, *Appl. Phys. Lett.* **109**, 131105 (2016).
- [12] T. Tajima and J. M. Dawson, *Phys. Rev. Lett.* **43**, 267 (1979).
- [13] W. P. Leemans *et al.*, *Phys. Rev. Lett.* **91**, 074802 (2003).
- [14] W. P. Leemans, J. van Tilborg, J. Faure, C. G. R. Geddes, C. Tóth, C. B. Schroeder, E. Esarey, G. Fubiani, and G. Dugan, *Phys. Plasmas* **11**, 2899 (2004).
- [15] J. Déchard, A. Debayle, X. Davoine, L. Gremillet, and L. Bergé, *Phys. Rev. Lett.* **120**, 144801 (2018).
- [16] A. Gopal, P. Singh, P. Herzer, S. Reinhard, A. Schmidt, U. Dillner, T. May, H.-G. Meyer, W. Z. W., and G. G. Paulus, *Opt. Lett.* **38**, 4705 (2013).
- [17] G. Liao *et al.*, *Proc. Nat. Ac. Sci.* **5**, 3994 (2019).
- [18] D. Kartashov, S. Ališauskas, A. Pugžlys, A. Voronin, A. Zheltikov, M. Petrarca, P. Béjot, J. Kasparian, J.-P. Wolf, and A. Baltuška, *Opt. Lett.* **16**, 3456 (2012).
- [19] D. Woodbury *et al.*, *Opt. Lett.* **43**, 1131 (2018).
- [20] S. Tochitsky *et al.*, *Nat. Photonics* **13**, 41 (2018).
- [21] I. Pogorelsky, M. Polyanskiy, and W. D. Kimura, *Phys. Rev. Acc. Beams* **19**, 091001 (2016).
- [22] M. Clerici *et al.*, *Phys. Rev. Lett.* **110**, 253901 (2013).
- [23] A. Nguyen, P. González de Alaiza Martínez, I. Thiele, S. Skupin, and L. Bergé, *Phys. Rev. A* **97**, 063839 (2018).
- [24] V. Y. Fedorov and S. Tzortzakakis, *Opt. Express* **26**, 31150 (2018).
- [25] V. A. Tulskey, M. Bagheri, U. Saalman, and S. V. Popruzhenko, *Phys. Rev. A* **98**, 053415 (2018).
- [26] E. Lefebvre *et al.*, *Nucl. Fusion* **43**, 629 (2003).
- [27] P. González de Alaiza Martínez, X. Davoine, A. Debayle, L. Gremillet, and L. Bergé, *Scientific Reports* **6**, 26743 (2016).
- [28] M. V. Ammosov, N. B. Delone, and V. P. Krainov, *Sov. Phys. JETP* **64**, 1191 (1986).
- [29] See Supplemental Material for complementary results on the 1D model, Biot-Savart solution and spectral analysis.
- [30] A. Debayle, L. Gremillet, L. Bergé, and C. Köhler, *Opt. Express* **22**, 13691 (2014).
- [31] W. B. Mori and T. Katsouleas, *Phys. Rev. Lett.* **69**, 3495 (1992).
- [32] W. B. Mori, *IEEE Journal of Quantum Electronics* **33**, 1942 (1997).
- [33] D. F. Gordon, B. Hafizi, P. Sprangle, R. F. Hubbard, J. R. Peñano, and W. B. Mori, *Phys. Rev. E* **64**, 046404 (2001).
- [34] W. Lu, M. Tzoufras, C. Joshi, F. S. Tsung, W. B. Mori, J. Vieira, R. A. Fonseca, and L. O. Silva, *Phys. Rev. ST Accel. Beams* **10**, 061301 (2007).
- [35] O. Kosareva *et al.*, *Opt. Lett.* **43**, 90 (2018).
- [36] N. J. Carron, *Prog. Electrom. Res.* **28**, 147 (2000).